

There Is More to Outshining: 2D Dust Effects on Stellar Mass Estimates at $3 \leq z < 9$ with JWST in the JADES Field

M. Hamed¹ , P. G. Pérez-González¹, M. Annunziatella², L. Colina¹, I. Shvai¹, M. Perna¹, A.J. Bunker³, K. Małek^{4,5}, S. Arribas¹, J. Álvarez-Márquez¹, C.N.A. Willmer⁶, H. Übler⁷, R. Bhatawdekar⁸, J. Chevallard³, E. Curtis-Lake⁹, Z. Ji⁶, P. Rinaldi¹⁰, and C.C. Williams¹¹

¹ Centro de Astrobiología (CAB), CSIC-INTA, Ctra. de Ajalvir km 4, Torrejón de Ardoz, E-28850, Madrid, Spain

² INAF – IASF Milano, Via A. Corti 12, 20133 Milano, Italy

³ Department of Physics, University of Oxford, Denys Wilkinson Building, Keble Road, Oxford OX1 3RH, UK

⁴ National Centre for Nuclear Research, Pasteura 7, 02-093, Warsaw, Poland

⁵ Aix Marseille Univ. CNRS, CNES, LAM, Marseille, France

⁶ Steward Observatory, University of Arizona, 933 N. Cherry Avenue, Tucson, AZ 85721, USA

⁷ Max-Planck-Institut für extraterrestrische Physik (MPE), Gießenbachstraße 1, 85748 Garching, Germany

⁸ European Space Agency (ESA), European Space Astronomy Centre (ESAC), Camino Bajo del Castillo s/n, 28692 Villanueva de la Cañada, Madrid, Spain

⁹ Centre for Astrophysics Research, Department of Physics, Astronomy and Mathematics, University of Hertfordshire, Hatfield AL10 9AB, UK

¹⁰ Space Telescope Science Institute, 3700 San Martin Drive, Baltimore, Maryland 21218, USA

¹¹ NSF National Optical-Infrared Astronomy Research Laboratory, 950 North Cherry Avenue, Tucson, AZ 85719, USA

ABSTRACT

Aims. Dust attenuation modifies the observed spectral energy distribution (SED), leading to biases in the physical parameters inferred from integrated SED fitting linked to degeneracies (e.g., between dust content and age). As spatially resolved SED modeling becomes feasible for large high-redshift samples, it is increasingly important to assess how dust attenuation affects resolved mass estimates. We evaluate the impact of dust attenuation on stellar mass estimates derived from integrating spatially resolved SED fitting results.

Methods. We perform spatially resolved and integrated SED fitting on a sample of 3 408 galaxies at $3 \leq z < 9$ from the Great Observatories Origins Deep Survey (GOODS) South field, combining deep NIRCam from the JWST Advanced Deep Extragalactic Survey (JADES) and HST/ACS imaging from GOODS and the Cosmic Assembly Near-infrared Deep Extragalactic Legacy Survey (CANDELS). We compare galaxy-integrated properties derived from fitting the summed SED with those obtained from spatially resolved SED modeling. Using a two-component dust attenuation model with a variable slope, we investigate how the dust attenuation slope, A_V , and stellar population properties contribute to discrepancies in the resulting stellar mass estimates.

Results. Resolved stellar masses are systematically higher than integrated estimates, with a median offset of $\Delta \log M_\star = +0.24$ dex. This offset exhibits a strong mass dependence: $+0.34$ dex at low masses ($\log M_\star/M_\odot < 8$), decreasing to $+0.22$ dex at intermediate masses ($\log M_\star/M_\odot \sim 8.5$), and approaching agreement ($+0.04$ dex) at the highest masses ($\log M_\star/M_\odot > 10$). This demonstrates that outshining, where young stellar populations dominate the integrated light, disproportionately affects low-mass galaxies and leads to mass underestimation by factors of ~ 2 . Resolved analyses recover higher dust attenuations ($\Delta A_V \approx +0.08$ mag), lower birth cloud (BC) fractions ($\Delta \mu \approx -0.28$, with $\mu \equiv \frac{A_{VISM}}{A_{VBC}+A_{VISM}}$), and grayer attenuation curves ($\Delta \delta_{ISM} = +0.08$), arising from preferential sampling of compact star-forming regions. Integrated fits underestimate stellar ages by $\sim 23\%$ at $z < 5$ and 31% at $z \gtrsim 5$. The stellar mass offset correlates strongly with the age difference ($r = 0.78$) and the attenuation slope difference ($r = 0.84$), indicating that age-dependent outshining and spatially varying dust geometry are primary drivers of the discrepancy between resolved and integrated stellar masses.

Use \titlerunning to supply a shorter title and/or \authorrunning to supply a shorter list of authors.

1. Introduction

Since its launch and first light earlier this decade, the James Webb Space Telescope (JWST) has been transforming our understanding of early galaxy evolution by enabling observations of rest-frame optical light at high redshifts (e.g., [Finkelstein et al. 2022](#); [Castellano et al. 2022](#); [Naidu et al. 2022](#); [Yan et al. 2023](#); [Adams et al. 2023](#); [Álvarez-Márquez et al. 2023](#); [Finkelstein et al. 2023](#); [Gómez-Guijarro et al. 2023](#); [Bunker et al. 2023](#); [Sabti et al. 2024](#); [Navarro-Carrera et al. 2024](#); [Martorano et al. 2025](#); [Pérez-González et al. 2025](#)). These observations have uncovered the underlying stellar mass and older stellar populations that remained largely obscured in earlier data from the Hubble Space Telescope (HST).

The synergy between JWST and HST now enables a more complete view of galaxies in the early Universe. HST's rest-frame ultraviolet (UV) imaging captures unattenuated star formation in galaxies beyond the cosmic noon, while the optical and near-infrared (NIR) capabilities of JWST probe obscured star formation and the evolved stellar component. At $z > 3$, the combination of UV and optical/NIR coverage is essential for breaking degeneracies between stellar age and dust attenuation. (e.g., [Wang et al. 2024](#); [Iani et al. 2024](#); [Weibel et al. 2024](#); [Li et al. 2024](#)).

Together, the high spatial resolution of JWST and HST have opened a new window into the internal structure of high-redshift galaxies. HST provided some of the first resolved views of star-forming regions in the rest-frame UV ([Abraham et al. 1999](#);

Lanyon-Foster et al. 2012; Wuys et al. 2013; Morishita et al. 2015; Abdurro’uf & Akiyama 2018; Jafariyazani et al. 2019; Lee et al. 2022), while JWST extends this capability into the rest-frame optical and NIR, enabling spatially resolved mapping of stellar populations and star formation activity (Polletta et al. 2024; Matharu et al. 2024). Crucially, JWST allows for pixel-by-pixel (resolved) spectral energy distribution (SED) fitting across a broad wavelength range, capturing internal gradients and revealing sub-galactic variations in physical properties (Wang et al. 2022; Song et al. 2023; Giménez-Arteaga et al. 2023; Pérez-González et al. 2023; D’Eugenio et al. 2024).

While resolved SED fitting with JWST represents a major leap forward in mapping internal physical properties of high-redshift galaxies, mounting evidence indicates that resolved and integrated SED fitting often yield systematically different stellar mass estimates (Zibetti et al. 2009; Sorba & Sawicki 2015, 2018; Pérez-González et al. 2023; Giménez-Arteaga et al. 2023, 2024; Lines et al. 2025). One primary mechanism driving these discrepancies is outshining (Papovich et al. 2001; Conroy 2013; Sorba & Sawicki 2018; Tacchella et al. 2022; Topping et al. 2022; Suess et al. 2022; Whiter et al. 2023; Narayanan et al. 2024; Witten et al. 2025). This effect arises when the luminous emission from young, massive stars dominates the integrated light, effectively masking the fainter contribution from older stellar populations, and thereby hindering accurate stellar mass estimates. Numerous studies have compared stellar masses derived from resolved and integrated photometry. While some report good agreement between the two approaches (e.g., Hemmati et al. 2014; Cibinel et al. 2015; Pérez-González et al. 2023; Shen et al. 2024; Li et al. 2024; Lines et al. 2025), others highlight that integrated SED fitting can systematically underestimate stellar mass due to outshining (e.g., Pforr et al. 2012; Sorba & Sawicki 2018; Giménez-Arteaga et al. 2023). Resolved SED fitting mitigates this bias by spatially disentangling star-forming regions from older stellar populations, which enables a more accurate reconstruction of the total stellar mass.

Assumptions about the star formation history (SFH) in SED fitting have been shown to significantly influence the severity of outshining-induced biases in stellar mass estimates (Gallazzi & Bell 2009; Bolzonella et al. 2010; Wuys et al. 2013; Sorba & Sawicki 2015; Narayanan et al. 2024; Jain et al. 2024). Simplified parametric forms, such as exponentially declining SFHs, tend to overemphasize recent star formation activity, which in turn leads to systematic underestimation of both stellar masses and mass-weighted ages (Narayanan et al. 2024; Jain et al. 2024). Similarly, Giménez-Arteaga et al. (2024) found that single-component SFH models can underestimate the total stellar mass by up to 0.5 dex, whereas adopting a two-component SFH leads to better agreement with resolved measurements. Narayanan et al. (2024) showed that rigid SFH models fail to recover early star formation episodes when the observed light is dominated by recent bursts, and found that these biases can be mitigated by adopting flexible SFHs, that better reflect the diversity of star formation histories seen in high redshift galaxies (Looser et al. 2025; Lisiecki et al. 2025).

While the influence of SFH on outshining and stellar mass biases has been widely explored (e.g., García-Argumánez et al. 2023), the role of dust attenuation in this context remains less understood. Dust attenuation occurs when interstellar dust grains absorb a substantial fraction of the UV and optical photons, predominantly emitted by young, massive stars, and

re-emit this energy thermally in the infrared (IR), effectively redistributing the stellar radiation across the electromagnetic spectrum. The dust attenuation law has been shown to vary between galaxies (i.e., is non-universal) (Kriek & Conroy 2013; Battisti et al. 2016; Lo Faro et al. 2017; Salim et al. 2018; Małek et al. 2018; Buat et al. 2019; Hamed et al. 2023a; Markov et al. 2025; Shvaei et al. 2025). The effect of dust attenuation on the SED of a galaxy, and therefore on the inferred physical properties, is influenced by various physical factors, such as dust composition (Di Mascia et al. 2021), metallicity (Shvaei et al. 2020a,b; Hamed et al. 2023b), and the relative distribution of stars and dust (Buat et al. 2019; Hamed et al. 2023a), all of which can shape the attenuation curve (Calzetti et al. 2000; Charlot & Fall 2000; Narayanan et al. 2018; Salim & Narayanan 2020).

Given that both dust attenuation and SFH influence the relative visibility of young and old stellar populations, their combined effect may amplify or mitigate the outshining bias. This motivates a systematic investigation of how variations in dust attenuation properties affect the discrepancies between resolved and integrated stellar mass estimates, particularly in galaxies observed with JWST at high redshift.

Although previous spatially resolved studies have provided important insights, many focused on individual systems (e.g., Giménez-Arteaga et al. 2023), limited to narrow redshift ranges (e.g., Wang et al. 2022), or biased toward the most massive galaxies (e.g., Pérez-González et al. 2023). In this paper, we aim to analyze a statistically significant, mass-complete sample of galaxies across a wide redshift range ($3 \leq z < 9$), enabling a robust assessment of stellar mass estimation through resolved and integrated SED fitting, and the role dust attenuation plays in shaping these measurements. Using spatially resolved SED modeling based on JWST/NIRCam and HST/ACS imaging in the GOODS-South field, we specifically investigate how variations in the attenuation slope, and dust attenuation properties, correlate with discrepancies between resolved and integrated stellar mass estimates.

This paper is structured as follows. In Section 2, we describe the data used in this work, as well as the sample selection criteria. In Section 2.2, we describe the methods used in handling our data and processing the maps, such as matching the point spread functions (PSF) of the different bands in order to perform the resolved analysis. The techniques employed for the integrated and resolved SED fitting are presented in Section 3. The results are presented in Section 4, and they are discussed and summarized in Section 5.

Throughout this paper, we adopt a flat Λ CDM cosmology with $\Omega_M = 0.3$, $\Omega_\Lambda = 0.7$, and a Hubble constant of $H_0 = 70 \text{ km s}^{-1} \text{ Mpc}^{-1}$. Stellar masses and SED modeling are computed assuming a Chabrier (2003) initial mass function (IMF).

2. Dataset and sample selection

2.1. Sample description

The sample used in this paper has been assembled from the Astrodeep-JWST catalogue (Merlin et al. 2024), in the Great Observatories Origins Deep Survey (GOODS, Giavalisco et al. 2004) South field (Beckwith et al. 2006). This catalogue provides source detection and photometry on JWST NIRCam

imaging mosaics from the JWST Advanced Deep Extragalactic Survey (JADES, Eisenstein et al. 2023; Rieke et al. 2023; Eisenstein et al. 2025) Data Releases 1 and 2. The JADES imaging provides exceptional depth, reaching a 5σ point-source detection limit of $m_{AB} \approx 30$ mag in the F200W filter in the Deep regions (Rieke et al. 2023; Eisenstein et al. 2025). The GOODS-South field was selected due to its extensive multi-wavelength coverage and the availability of deep archival data, which is ideal for resolved studies of galaxies across cosmic time. Since our primary goal is to investigate how dust attenuation affects the discrepancies between resolved and integrated properties, particularly stellar mass estimates, we leverage the complementary capabilities of JWST and HST in this well-characterized field. This dataset allows us to probe both the rest-frame UV and optical emission of galaxies at high redshift.

The NIRCam mosaics for the GOODS-South region are drawn from the JADES program’s Guaranteed Time Observation (GTO), specifically programs 1180 (PI: Eisenstein) and 1210 (PI: Luetzendorf). In Astrodeep-JWST, NIRCam observations were supplemented with imaging from the Hubble Legacy Fields (HLF, Illingworth et al. 2016). This combines deep ACS/WFC imaging with NIRCam wide and medium bands for a total of eighteen broadbands (fourteen NIRCam bands and four ACS/WFC) spanning from 0.4 to $5 \mu\text{m}$ (Illingworth et al. 2016; Oesch et al. 2023; Williams et al. 2023). All the maps were calibrated and drizzled to match the same angular scale of $0.03''$ per pixel. The Astrodeep-JWST catalog for the GOODS-South field contains 73 638 galaxies, with photometric redshifts computed as the mean of the two central values from four estimates: one from ZPHOT (Fontana et al. 2000) and three from EAZY (Brammer et al. 2008), each using a different template configuration, to reach a reliable redshift estimation (Merlin et al. 2024).

In the Astrodeep-JWST catalogue, Merlin et al. (2024) measured photometry on PSF-matched images using fixed circular apertures, from which an optimal aperture is selected per source based on its segmentation area. This ensured robust total flux estimates for each galaxy in the parent sample.

To enable a comprehensive study of resolved physical properties, with a particular focus on dust attenuation effects, we adopted an inclusive sample selection strategy. Rather than applying strict cuts for representativeness, we prioritized ensuring sufficient photometric coverage for reliable SED fitting. Specifically, we required each galaxy to have detections in at least four photometric bands with a minimum signal-to-noise ratio (S/N) of 3σ in each. This criterion resulted in 54 125 galaxies selected from the parent sample. To ensure adequate sampling of the rest-frame UV and optical spectrum which is crucial for reliably constraining stellar ages, dust attenuation, and stellar masses (Walcher et al. 2011), we adopted a minimum redshift cut of $z = 3$. At these redshifts, the combined wavelength coverage of HST/ACS (0.4–0.8 μm) and JWST/NIRCam (0.9–5 μm) maps onto the rest-frame UV–optical window. This enables robust recovery of stellar population parameters, including the UV slope, the stellar ages, and mass. Applying this cut yields a sample of 13 094 galaxies. We do not impose a strict upper redshift cut beyond our S/N requirements in order to explore the feasibility of spatially resolved SED analysis toward the earliest cosmic epochs. Our full sample reaches a maximum redshift of $z = 8.8$.

We then selected a stellar mass-complete subsample, by following the approach outlined by Pozzetti et al. (2010), which estimates the limiting stellar mass for each galaxy based on its observed magnitude. Specifically, for each source, we calculate a limiting mass defined as the stellar mass a galaxy would have if its apparent magnitude were equal to the limiting magnitude of the survey in the F444W band. For each redshift bin, we identify the stellar mass above which 90% of galaxies exceed M_{lim} and adopt this as the 90% stellar mass completeness limit. This defines a mass-complete subsample for subsequent analysis while minimizing selection biases. The stellar masses for mass-completeness selection were obtained from Merlin et al. (2024). Applying these criteria results in a sample of 3 415 galaxies, complete down to $\log(M_{\star}/M_{\odot}) = 7.5$.

To minimize contamination from active galactic nuclei (AGN) emission, we cross-matched our sample with the Chandra Deep Field South X-ray catalog (Luo et al. 2017), identifying 19 X-ray sources. Of these, we excluded 7 bright AGN (intrinsic X-ray luminosity $L_X > 10^{44} \text{ erg s}^{-1}$) to prevent contamination of the stellar population fits, while retaining 12 sources with lower X-ray luminosities where AGN emission is expected to be negligible in the observed optical/NIR bands. We acknowledge that X-ray selection may not capture all AGN at high redshift (Maiolino et al. 2025). Our X-ray based AGN exclusion therefore represents a conservative approach that removes only the most luminous AGN, while lower-luminosity or X-ray weak AGN may remain in the sample. However, given that our sample is mass-complete and dominated by star-forming galaxies (98% within the main sequence), any residual AGN contamination is expected to be minimal. This resulted in a final sample of 3 408 galaxies, which form the basis for our study of both resolved and integrated SED properties. Figure 1 presents the main characteristics of the sample, including its redshift distribution, stellar masses, and offset from the star forming main sequence. The vast majority of galaxies (98%) lie within the main sequence defined by Speagle et al. (2014).

For the purposes of our analysis, we divide the sample into two redshift bins: $3 \leq z < 5$ and $5 \leq z$. This division reflects the evolving rest-frame wavelength coverage of the photometry with redshift. At $z > 5$, the reddest available band no longer probes the rest-frame NIR, which limits our sensitivity to the oldest stellar populations and can affect the robustness of stellar mass estimates. Our full sample reaches a maximum redshift of $z = 8.8$, with a median redshift of $z = 3.6$. The redshift interquartile range (middle 50% of the distribution) is $3.4 < z < 4.3$, and 90% of galaxies lie below $z = 5.2$. In total, 383 galaxies lie in the $5 \leq z < 9$ bin (with interquartile in $5.3 < z < 6.2$), while the remaining galaxies fall within $3 \leq z < 5$ (with interquartile being $3.3 < z < 3.9$).

2.2. Map processing

To ensure consistent spatial resolution across all photometric bands prior to the resolved SED fitting, we performed PSF matching to the broadest NIRCam filter (F444W), which has the largest full width at half maximum (FWHM) measured in our images ($0.16''$). Empirical PSFs were constructed for each band using Photutils (Bradley et al. 2024) by identifying and stacking isolated, unsaturated stars in the field. On average, 47 stars were selected independently per band to account for wavelength-dependent PSF variations, proper motions between epochs, and filter-specific detection limits. Each star was centered, normalized, and the final PSF was built as the weighted

mean of the stack. To suppress noise from PSF wings and focus on the core structure, a circular mask was applied during stacking (as done in Pérez-González et al. 2023).

We convolved each image to the F444W resolution using a custom-built kernel derived in Fourier space from the empirical PSFs. This method accelerates computation and maintains kernel accuracy. The choice of a tapering function is crucial in building the kernels, as it controls how the transformation is applied in Fourier space (Martinache et al. 2020). We adopted a split cosine bell tapering function (Berkheimer et al. 2024; Matsuura et al. 2024), which preserved the extended PSF structures. The split cosine bell function has two tapering parameters: α (defining the width of the flat central region) and β (controlling the width of the transition region).

Unlike a sharp frequency cutoff, which can introduce ringing artifacts, the split cosine bell provided a smooth transition to zero, preserving the core structure of the PSF while suppressing noisy components in the wings. This is especially important when matching heterogeneous datasets, such as HST to JWST or between NIRCam filters, where differences in spatial resolution and detector response can lead to significant variation in PSF structure. We found that varying α between 0.4 and 0.6, and β between 0.1 and 0.3 produced optimal results. The final FWHM of the convolved images were checked using the same stars, matching the FWHM measured for F444W.

We then measured photometry on a pixel-by-pixel basis using the PSF-matched JWST and HST maps (with a pixel scale corresponding to 0.03 arcsec per pixel), while measuring their noise empirically in source free regions of the original cutouts, to avoid the noise correlation introduced by the convolution. While correlated noise is still present at some level in the drizzled mosaics due to resampling, this effect is not explicitly corrected for. For the resolved SED fitting, we retained only those pixels that had at least a S/N of three in at least four photometric bands (Pérez-González et al. 2023). This mild criterion ensures that the resolved SED fitting is performed reliably only on pixels with sufficient photometric coverage. This pixel selection resulted in 138 pixels per galaxy on average. Given the matched PSF FWHM of 0.16" and pixel scale of 0.03"/pixel, this corresponds to approximately 6 independent spatial resolution elements per galaxy. To ensure a fair comparison with integrated measurements, we quantified the area covered by the pixels used in the resolved analysis relative to the total aperture adopted for each galaxy. On average, the selected pixels cover 35% of the total aperture area measured by Merlin et al. (2024), with an interquartile range of 29–40%, and extending up to 46% at the 90th percentile across the sample. These pixels correspond to the brightest, high-S/N regions where the spatially resolved SED fits are most reliable. Despite representing only about one-third of the total aperture area, these regions recover a large fraction of the total flux: the ratio between the recovered and integrated fluxes has a median of 0.68, with an interquartile range of 0.59–0.76. The stellar masses derived from the resolved and integrated analysis (Section 3) were scaled by the corresponding aperture correction factors, which have a median value of 1.47 (with an interquartile range of 1.30–1.68) to account for the fraction of the total aperture not covered by the pixels used in the resolved analysis. This ensures that the total stellar masses reflect the full galaxy flux.

3. Spectral energy distribution modeling

3.1. Spatially resolved SED fitting

Traditionally, SED fitting has been performed on the integrated light of galaxies, treating them as spatially uniform systems. However, this approach overlooks internal variations in stellar populations, star formation, and dust content. Spatially resolved SED fitting, conducted on a pixel-by-pixel basis, provides a more detailed view of the underlying physical processes by capturing sub-galactic gradients in age, mass, and attenuation (García-Argumánez et al. 2023; Giménez-Arteaga et al. 2023; Pérez-González et al. 2023). This method has become increasingly important for characterizing complex structures within galaxies.

To derive the spatially resolved physical properties of galaxies, we used the Code Investigating GALaxy Emission (CIGALE, version 2025, Boquien et al. 2019), which implements a Bayesian approach to SED fitting and allows flexible modeling of both star formation histories and attenuation laws. In this work, we configured CIGALE to model the stellar and dust emission of each spatial element using a range of physically motivated templates. The code allows for a modular construction of the SED, which enables the combination of different SFHs, attenuation laws, and nebular emission components. Below, we describe the specific modules and parameter choices adopted for our analysis.

3.1.1. Stellar component

To model the stellar emission, we adopted the Bruzual & Charlot (2003) single stellar population models, allowing metallicities to range from $0.01 \times Z_\odot$ up to Z_\odot . This was done to capture the internal diversity of galaxy regions (e.g., localized star-forming regions with sub-solar metallicities, and evolved regions with near-solar ones). Metallicity might influence the shape of the stellar continuum, particularly in the optical–NIR, therefore restricting metallicity to a narrow range (e.g., fixed solar) can lead to biased estimates of physical parameters (Maraston et al. 2010). Additionally, we accounted for nebular continuum and line emission in our SED fitting, since it is crucial in UV–optical bands, especially for young star-forming regions and high redshift galaxies (Boquien et al. 2010; de Barros et al. 2014).

A fundamental component of SED fitting is the SFH, as it governs the relative contribution of stellar populations of different ages and directly influences derived physical properties such as stellar mass, age, and star formation rate (Wuyts et al. 2012; Conroy 2013; Ciesla et al. 2016). For this work, where our primary objective is to understand how dust attenuation influences stellar mass estimates in resolved fits, we performed a systematic exploration of several commonly adopted parametric SFH forms, including constant, delayed exponentially declining ($SFR(t) \propto t \times \exp(-t/\tau)$), and delayed with a recent burst within the last 100 Myr.

We assessed the performance of each SFH model by comparing the resolved and integrated stellar masses, as well as the corresponding SEDs and reduced χ^2 values. We find that the adopted SFH exerts an important influence on the derived stellar masses, particularly at lower stellar masses where recent star formation dominates the integrated light. Models assuming shorter minimum stellar ages or bursty histories tend to yield slightly larger mass discrepancies, consistent with the stronger

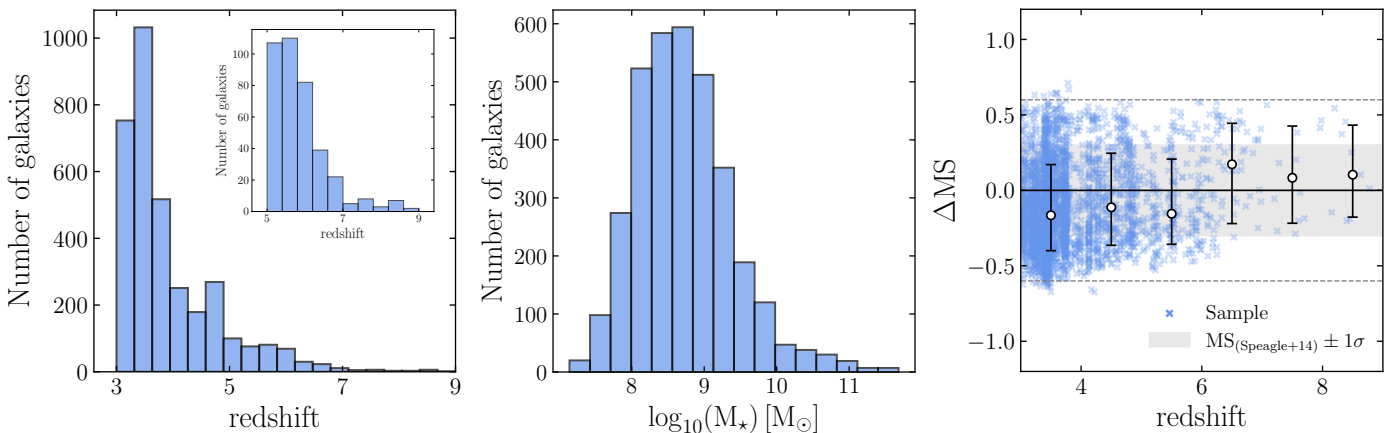


Fig. 1. Characterization of the galaxy sample used in this work. **Left:** redshift distribution of the sample. The distribution at $5 \leq z < 9$ is magnified in the inset for better visualization. **Middle:** distribution of stellar masses derived from SED fitting based on aperture-photometry fluxes for the sample from Merlin et al. (2024). **Right:** offset from the star-forming main sequence, defined as $\Delta MS = \log(SFR_{\text{SED}}) - \log(SFR_{\text{MS}}(M_*, z))$, as a function of redshift, computed relative to the evolving main-sequence relation of Speagle et al. (2014). Black circles indicate binned medians with 16th–84th percentile ranges. The shaded region denotes the $\pm 1\sigma$ intrinsic scatter of the main sequence, and the dashed lines mark the ± 0.6 dex thresholds commonly used to separate starburst and quiescent regimes.

impact of outshining by young stellar populations. Although the overall systematic offset between resolved and integrated estimates persists across all SFH assumptions, the amplitude and scatter of $\Delta \log M_*$ vary with the chosen SFH, underscoring the importance of the star-formation history in shaping the inferred stellar masses.

As described in Appendix A, we tested several SFH parametrizations including constant, delayed exponentially declining, and delayed with a recent burst, as well as different minimum stellar ages in the SSP models (10, 25, 50, and 100 Myr). This minimum stellar ages in the SSP models refer to the youngest simple stellar population age available in the model grid. The choice of SFH introduces systematic offsets in the resolved-to-integrated stellar mass difference $\Delta \log M_*$: median values range from 0.16 dex (delayed + burst) to 0.30 dex (constant SFH with 10 Myr minimum age), with a maximum variation of 0.14 dex across all tested configurations. We adopted a constant SFH with a minimum stellar age of 50 Myr, which yields an intermediate systematic offset of 0.24 dex and the lowest scatter ($\sigma = 0.18$ dex) among all tested models. This choice balances computational efficiency while avoiding unrealistically young stellar populations that could enhance outshining bias, and preserves robust stellar mass estimates. The constant SFH, despite its simplicity, has been shown to yield reliable stellar masses in spatially resolved analyses (e.g., Giménez-Arteaga et al. 2023; Lines et al. 2025).

3.1.2. Dust component

Interstellar dust affects the studied wavelength regime in this work via the dust attenuation. Modeling dust attenuation is a crucial component of SED fitting, particularly for high-redshift galaxies, where dusty star-forming regions dominate UV and optical light. Despite major advancements in attenuation modeling, key challenges remain, especially in disentangling age and dust effects, understanding the geometry of stars and dust, and constraining the properties of the oldest stellar populations.

Dust attenuation in galaxies is often described using either empirical prescriptions or more physically motivated models. The widely used Calzetti et al. (2000) law treats attenuation as arising from a uniform foreground dust screen, providing a good empirical fit to the integrated light of typical star-forming galaxies (e.g., Buat et al. 2012; Malek et al. 2017; Elbaz et al. 2018; Ciesla et al. 2020; Hamed et al. 2021). However, this formalism lacks the flexibility to capture the greyer attenuation curves expected in systems with complex star-dust geometries, where age-dependent obscuration and spatial mixing become important (e.g., Noll et al. 2009; Buat et al. 2019; Salim & Narayanan 2020).

To better account for these complexities, we adopt the two-component dust attenuation model introduced by Charlot & Fall (2000). In this framework, stars younger than a characteristic timescale, set to 10 Myr, corresponding to the dispersal time of their natal birth clouds (BCs), are attenuated by both the dense BCs and the diffuse interstellar medium (ISM), while older stars experience attenuation from the ISM only. This age-dependent treatment reflects the physical distinction between newly formed stars embedded in their birth environments and the older stellar populations dispersed throughout the galaxy.

The attenuation at each wavelength is modeled using power-law functions for each component:

$$A_\lambda(t) = A_V^{\text{ISM}} \left(\frac{\lambda}{5500 \text{ \AA}} \right)^{\delta_{\text{ISM}}} + \begin{cases} A_V^{\text{BC}} \left(\frac{\lambda}{5500 \text{ \AA}} \right)^{\delta_{\text{BC}}}, & \text{if } t < 10 \text{ Myr} \\ 0, & \text{if } t \geq 10 \text{ Myr} \end{cases} \quad (1)$$

Here, A_V^{ISM} and A_V^{BC} are the V-band attenuations in the ISM and BC components, respectively, while δ_{ISM} and δ_{BC} control the steepness of the attenuation curve for each component. The relative contribution of the ISM and BC is parameterized by $\mu = A_V^{\text{ISM}} / (A_V^{\text{ISM}} + A_V^{\text{BC}})$. The variable t denotes the stellar age, and 10 Myr is the characteristic timescale for birth cloud dispersal.

Table 1. List of input parameters for SED modeling with CIGALE. The parameter values shown here correspond to those of the final computation of the SEDs, after testing different value ranges. The values are linearly equally spaced.

Parameter	Priors
Constant SFH	
Age _★ [Myr]	100 values in [50-2000]
Nebular emission (Inoue 2011)	
Ionization parameter ($\log U$)	-3, -2, -1
SSP (Bruzual & Charlot 2003)	
IMF	(Chabrier 2003)
Z_*	3 values in $[Z_\odot/100, Z_\odot]$
Separation age ⁱ	10 Myr
Dust attenuation (modified Charlot & Fall 2000)	
$A(V)_{\text{ISM}}$	100 values in [0-3]
μ^{ii}	7 values in [0.3-1]
δ_{ISM}	7 values in [-1.5, -0.3]

ⁱ The separation age defines the threshold below which young stars are attenuated by both BC and the ISM, while older stars are only affected by ISM attenuation.

ⁱⁱ $A_V^{\text{ISM}} / (A_V^{\text{BC}} + A_V^{\text{ISM}})$.

We fix the slope of the birth cloud component to $\delta_{\text{BC}} = -1.3$, a steep value consistent with the highly embedded environments around young stars (as in e.g., Wild et al. 2007; da Cunha et al. 2008; Chevallard et al. 2013). In contrast, the ISM slope δ_{ISM} is left as a free parameter to capture spatial variations in dust properties. The original Charlot & Fall (2000) model adopted a fixed $\delta_{\text{ISM}} = -0.7$ to reproduce the average attenuation curve derived by Calzetti et al. (2000), but this fixed slope does not reflect the diversity of attenuation curves observed in galaxies. In particular, grayer attenuation curves that are linked to mixed geometries of stars and dust, have been reported in both local and high-redshift dusty galaxies (e.g., Pierini et al. 2004; Chevallard et al. 2013; Salim et al. 2018; Trayford et al. 2020). Allowing δ_{ISM} to vary enables us to explore such deviations and assess how the wavelength dependence of attenuation varies across different regions within galaxies.

3.2. Integrated SED fitting

To enable a direct comparison with our spatially resolved analysis, we performed integrated SED fitting by summing the photometric fluxes from the same set of PSF-matched pixels used in the resolved analysis. Specifically, we included only those pixels that met the predefined S/N threshold of 3σ in at least four bands. This approach mirrors the methodology used in previous resolved studies of high-redshift galaxies (e.g., Giménez-Arteaga et al. 2023). The stellar masses inferred from this integrated approach were also multiplied by the aperture correction factors discussed in Section 2.2. This ensured consistency between the resolved and integrated measurements by accounting for the flux outside the selected high S/N pixels. The resulting integrated SEDs thus represent the total emission within the same apertures adopted for the resolved analysis, which enables a one-to-one comparison of stellar masses derived from both methods. Appendix B illustrates these systematic

differences for an example galaxy, showing the spatial gradients in mass, age, and attenuation that integrated fitting averages over.

The SED fitting was carried out using the same configuration as in the resolved case, with the same set of templates, parameter priors, and physical assumptions. We adopted the Bruzual & Charlot (2003) stellar population models. Stellar metallicity was allowed to vary between sub-solar and solar values, and nebular emission lines were included. Dust attenuation was modeled using the Charlot & Fall (2000) double power law, with the attenuation slope in the diffuse ISM left as a free parameter to account for variations in dust geometry and composition. Table 1 shows the parameters used in both resolved and integrated SED fitting. By fitting the integrated SEDs with the same assumptions and selection criteria as the resolved fits, we are able to isolate the effects of spatial resolution and examine biases in the derived properties.

In the case of resolved SED fitting, physical properties were derived for each individual pixel. For the stellar mass and SFR, the values from all pixels within each galaxy were summed to obtain the total galaxy-integrated values, with uncertainties propagated in quadrature. Resolved mass-weighted stellar ages were computed as the mass-weighted mean across all pixels, $\langle \text{Age} \rangle_M = \sum_i (M_{\star,i} \times \text{Age}_i) / \sum_i M_{\star,i}$, where i indexes individual pixels. The resolved dust attenuation in the FUV and V bands were computed by summing the attenuated and unattenuated rest-frame luminosities from the best-fit SEDs at 150 nm and 550 nm across all the pixels within each galaxy. The total fluxes were then used to derive the band-specific attenuation as

$$A_\lambda^{\text{resolved}} = -2.5 \log_{10} \left(\frac{\sum_i F_{\lambda,i}^{\text{att}}}{\sum_i F_{\lambda,i}^{\text{int}}} \right), \quad (2)$$

where $F_{\lambda,i}^{\text{att}}$ is the attenuated flux of pixel i at wavelength λ , and $F_{\lambda,i}^{\text{int}}$ is the intrinsic (unattenuated) flux of pixel i . The uncertainty on $A_\lambda^{\text{resolved}}$ was derived using standard error propagation, assuming independence between pixel uncertainties.

To estimate the resolved attenuation curve slope of the ISM, we computed the attenuation contributed by the ISM component using the attenuated and unattenuated luminosities across all pixels in a set of broad-band filters spanning the rest-frame UV to NIR (150 to 1600 nm) as defined in Equation 2. This yielded a set of A_λ^{ISM} values as a function of wavelength. We then fitted these values using the functional form of the ISM attenuation law in Equation 1, treating the slope δ_{ISM} as a free parameter. This yields the ISM attenuation curve slope for each galaxy.

To estimate the resolved UV slope β (Calzetti et al. 1994), we computed the total rest-frame attenuated luminosities within ten narrow spectral windows spanning the wavelength range from 125 nm to 250 nm. These windows were selected to avoid strong spectral features and represent the underlying UV continuum (Finkelstein et al. 2012; Rogers et al. 2013). For each galaxy, we summed the attenuated fluxes of all valid pixels within each of the ten Calzetti windows. The UV slope β was then obtained by fitting a power-law $F_\lambda \propto \lambda^\beta$ to the total fluxes as a function of wavelength across the windows.

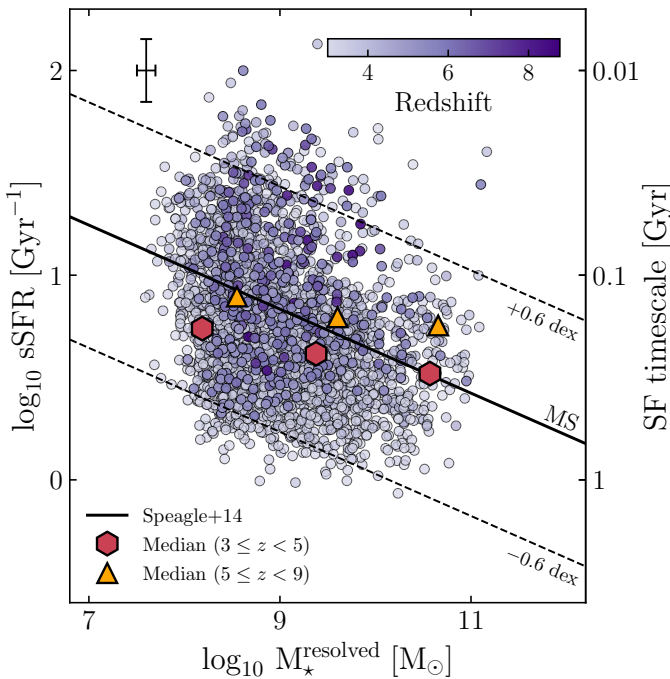


Fig. 2. Resolved specific star formation rate (sSFR) in Gyr^{-1} as a function of resolved stellar mass for the galaxy sample used in this work, color-coded by redshift. Each point represents an individual galaxy. The y-axis on the right side shows the corresponding star-formation timescale (1/sSFR) in Gyr. The solid black line indicates the star-forming main sequence (MS) from Speagle et al. (2014), evaluated at $z \approx 3.6$, while the dashed lines denote offsets of ± 0.6 dex (a factor of four) relative to the MS. Hexagonal and triangular symbols mark the median sSFR in bins of stellar mass for galaxies in the redshift ranges $3 \leq z < 5$ and $5 \leq z < 9$, respectively. The representative median measurement uncertainty in $\log M_\star$ and $\log \text{sSFR}$ is shown by the black error bar in the upper-left corner.

3.3. Model quality assessment

The quality of the SED fitting results was assessed using the reduced χ^2 statistic. This metric quantifies the agreement between the model and the observed photometry while accounting for photometric uncertainties and the number of fitted parameters. We first explored parameter grids and inspected posterior probability density functions to identify degeneracies and constrain priors, with particular attention to age and dust attenuation parameters. The final SED calculation included priors that are listed in Table 1. To evaluate the consistency of the resolved approach, we summed the best-fit pixel-by-pixel model SEDs and compared the resulting total fluxes to the integrated observed photometry in each band. We find a median reduced χ^2 of 1.79 for the resolved approach, compared to 0.80 for the integrated fits. The lower reduced χ^2 values in the integrated approach reflect the fact that it directly optimizes the fit to the total galaxy photometry, whereas the resolved approach sums independently fitted pixels, which does not guarantee a globally optimal solution for the integrated light.

To further evaluate the robustness of the derived physical parameters, we conducted a mock analysis (Osborne & Salim 2024) and present its results in Appendix C. This test assesses the ability of the adopted SED model configuration to recover input physical properties from synthetic photometry. The mock analysis confirms that key parameters such as stellar mass

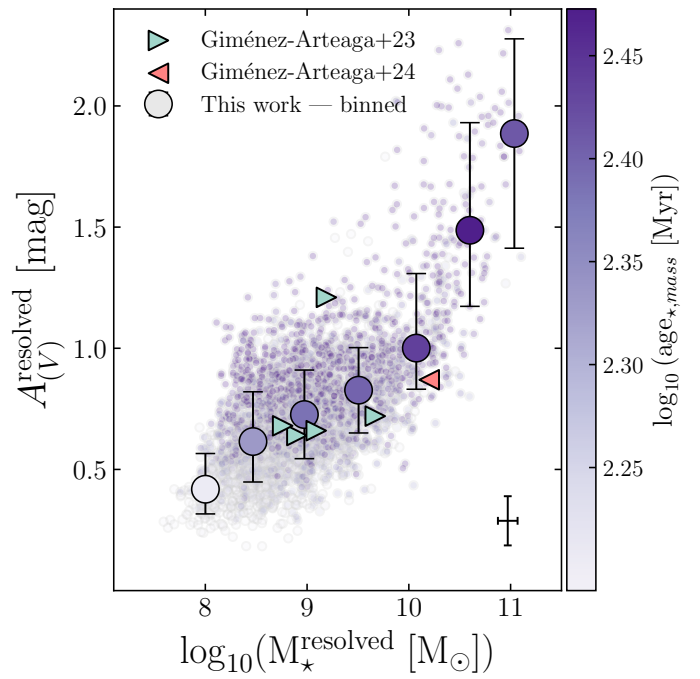


Fig. 3. Resolved dust attenuation $A(V)$ versus stellar mass, color-coded by mass-weighted stellar age. Large circles show binned medians with error bars indicating the 16th-84th percentile spread in $A(V)$. Literature comparisons from Giménez-Arteaga et al. (2023) (turquoise triangles) and Giménez-Arteaga et al. (2024) (red triangle) are shown for reference. The error bar in the lower-right corner represents median measurement uncertainties.

and SFR are reliably recovered, with small systematic offsets and tight correlations between the input and recovered values. These results validate the internal consistency of our SED modeling approach and highlight the strengths and limitations of parameter recovery under realistic observational conditions.

4. Results & Discussion

Following the SED fitting in Section 3, resolved and integrated estimates were derived for stellar mass, SFR, mass-weighted age, and attenuation properties. Median values and dispersions in redshift bins are summarized in Table 2. Figure 2 shows the relation between spatially resolved specific SFR (sSFR = SFR/M $_\star$) and stellar mass, colored by redshift, with the Speagle et al. (2014) main sequence used as the baseline. Here, SFR refers to the SED-derived instantaneous SFR, whereas the Speagle et al. (2014) relation is primarily calibrated using UV-based SFR indicators. The bulk of the sample lies within the main sequence band. Across the full sample, the median offset from the main sequence is $\Delta \log \text{sSFR} = -0.16$ dex, indicating that galaxies in our sample have slightly lower sSFR than predicted by the main sequence relation, with an interquartile range of 0.40 dex. The majority of galaxies (94.8%) fall within the main sequence boundaries defined by $-0.6 < \Delta \log(\text{sSFR}) < +0.6$ dex. Only a small fraction deviate significantly, with 2.7% classified as starbursts ($\Delta \log(\text{sSFR}) \geq +0.6$ dex) and 2.5% as quiescent systems ($\Delta \log(\text{sSFR}) \leq -0.6$ dex).

Figure 3 shows the relation between spatially resolved V-band attenuation (A_V) and stellar mass, color-coded by the mass-weighted stellar age. The attenuation increases steadily

with stellar mass, rising from $A_V \approx 0.4$ mag in the lowest-mass bins to ≈ 1.9 mag at the high-mass end. Across the full sample, the median attenuation is $\bar{A}_V = 0.73$ mag, with an interquartile range of 0.58–0.89 mag. Galaxies below $\log M_\star/M_\odot = 9.5$ show a median $A_V = 0.67$ mag, while those with $\log M_\star/M_\odot > 9.5$ have a median $A_V = 0.96$ mag. The observed ~ 0.3 mag scatter around the $A_V - M_\star$ relation might reflect variations in dust geometry and stellar population mixing rather than observational uncertainties. The overall trend of increasing attenuation with stellar mass is consistent with the consensus found in previous high-redshift studies. At $z \approx 2$ –3, [McLure et al. \(2018\)](#) showed that attenuation scales with stellar mass following a Calzetti-like law, with galaxies of $\log M_\star/M_\odot \gtrsim 9.5$ typically reaching $A_V \sim 1$ mag. Recent JWST-based analyses ([Markov et al. 2025](#)) extend this trend up to $z \sim 12$. The resolved $A_V - M_\star$ relation in Figure 3 closely follows the one-dimensional relation derived from the aperture-photometry SED fits. At the high-mass end, the higher attenuations partly reflect that the resolved A_V values are based on S/N-selected pixels, primarily sampling the bright central regions of galaxies, whereas the low-surface-brightness outskirts with lower attenuation are less represented in the measured flux-weighted attenuation. These results are also in agreement with [Giménez-Arteaga et al. \(2023\)](#) and [Giménez-Arteaga et al. \(2024\)](#), where they analyzed singular galaxies at $5 \leq z < 9$ star-forming galaxies.

4.1. Resolved versus integrated stellar masses

We summarize in Table 2 the median physical properties of our galaxy sample obtained from the spatially resolved and integrated SED fits across six redshift bins.

Figure 4 compares the stellar masses derived from the resolved and integrated SED fits, color-coded by resolved dust attenuation properties. The resolved fits systematically yield higher stellar masses, but the offset exhibits a strong mass dependence. At low masses ($7 < \log M_\star/M_\odot < 8$), the offset is $\Delta \log M_\star = +0.34$ dex. The offset decreases with increasing mass: $+0.22$ dex at $\log M_\star/M_\odot \sim 8.5$, $+0.21$ dex at $\log M_\star/M_\odot \sim 9.5$, and approaching the 1:1 relation ($+0.04$ dex) at the highest masses ($\log M_\star/M_\odot \sim 10.5$). This mass-dependent behavior is consistent at both low and high redshifts. The global median offset of $\Delta \log M_\star = +0.24^{+0.16}_{-0.17}$ dex is dominated by intermediate-mass galaxies ($\log M_\star \sim 8$ –10), which comprise 85% of the sample.

This mass-dependent trend demonstrates that outshining disproportionately affects low-mass galaxies. In these systems, a few bright young stellar populations can dominate the integrated light, causing integrated SED fits to underestimate the total stellar mass by factors of ~ 2 (0.3 dex at low masses). At higher masses ($\log M_\star > 10$), older stellar populations contribute more significantly to the integrated light, reducing the bias and bringing resolved and integrated estimates into agreement. This stellar mass offset is consistent with the differences reported for massive systems in [Pérez-González et al. \(2023\)](#) and at $z \sim 4$ –6 in [Lines et al. \(2025\)](#), where resolved and integrated stellar masses of normal star-forming galaxies agree within $\lesssim 0.3$ dex.

We note that the systematic underestimation of stellar masses by integrated SED fitting, particularly at $\log M_\star/M_\odot < 9$ where we find offsets of ~ 0.3 dex, may be relevant when interpreting black hole-to-stellar mass ratios at high redshift. Given that our X-ray-based AGN exclusion does not capture X-ray weak AGN ([Maiolino et al. 2025](#)), some fraction of our sample may host lower-luminosity AGN. In such cases, resolved stellar mass esti-

mates would provide more accurate measurements for assessing black hole scaling relations ([Pacucci et al. 2023](#)).

4.2. Dust attenuation and stellar population properties

The stellar mass offset is accompanied by systematic differences in dust attenuation properties and stellar ages (Table 2, Table 3). Resolved fits yield systematically higher A_V values with a median offset of $\Delta A_V \approx +0.08$ mag up to $z \sim 7$, lower μ ($\Delta \mu \approx -0.28$), and systematically older mass-weighted stellar ages. Relative to the resolved ages, the integrated fits underestimate stellar ages by approximately 25% at $z < 5$ and by 30% at $z \gtrsim 5$, corresponding to median absolute differences of $\Delta A_{\text{age, mass}} \approx 56$ Myr at lower redshifts and ≈ 35 Myr at higher redshifts.

The higher A_V values in resolved fits occur because they preferentially weight high surface brightness regions where young, attenuated stellar populations dominate the flux. These compact star-forming regions experience strong attenuation from both birth clouds and the diffuse ISM. In contrast, integrated SEDs average the light from both heavily attenuated central regions and less obscured outer regions, resulting in a lower effective A_V . The lower μ values ($\mu \equiv \frac{A_{V,\text{ISM}}}{A_{V,\text{BC}} + A_{V,\text{ISM}}}$, [Charlot & Fall 2000](#)) in the resolved fits further indicate that a larger fraction of the total attenuation arises in compact star-forming regions rather than in the diffuse ISM. In these regions, the optical depths are high ([Calzetti et al. 2000; Conroy 2013; Mitchell et al. 2013](#)), which increases the intrinsic mass-to-light ratios locally. These systematic differences in μ between resolved ($\mu \sim 0.45$) and integrated ($\mu \sim 0.72$) fits suggest that when fitting integrated SEDs without spatial information, adopting lower μ priors (around 0.4–0.5) may better account for the contribution of compact birth clouds that are spatially resolved in pixel-by-pixel analysis but averaged over in integrated fits. This could help mitigate the systematic underestimation of stellar masses in unresolved observations. The resolved attenuation slopes (δ_{ISM}) are slightly shallower than in the integrated SEDs ($\Delta \delta_{\text{ISM}} \approx 0.08$), reflecting that resolved fits preferentially sample compact, dusty regions where young stars are embedded in birth clouds (as indicated by lower μ values). In such clumpy, mixed star-dust geometries, the effective attenuation curve becomes grayer due to increased scattering and radiative transfer effects ([Trayford et al. 2020; Qin et al. 2024](#)). In contrast, integrated SEDs are averaged over regions with varying dust columns, producing steeper apparent slopes that dilute the contribution from birth clouds.

These results illustrate the combined effects of outshining ([Papovich et al. 2001; Conroy 2013; Narayanan et al. 2024](#)) and spatially varying dust attenuation on integrated SED estimates. When using integrated photometry to analyze the stellar content of galaxies, the total light is dominated by the bright, young, and less obscured stellar populations, which outshine the older and dustier components. This bias leads the integrated SED fits to infer systematically younger stellar ages, lower A_V , and smaller intrinsic mass-to-light ratios, resulting in an underestimation of the total stellar mass. The resolved analysis mitigates this effect ([Sorba & Sawicki 2015; Harvey et al. 2025](#)) by fitting each pixel independently, thus recovering the contribution from older, more attenuated stellar populations located in different regions of the galaxy. The resolved $A_V - M_\star$ relation in Figure 3 supports this interpretation, showing that within galaxies, regions of higher stellar mass exhibit stronger attenuation, consistent with dust being more concentrated in massive, central regions ([Wuyts et al. 2012; Tacchella et al. 2015](#)), which are downweighted in the in-

Table 2. Median physical properties of the galaxy sample in different redshift intervals, comparing the results from the spatially resolved and integrated SED fitting analyses. Reported values correspond to the median and the 16th–84th percentile range of the distribution (1σ scatter). Stellar masses and SFRs have been corrected for aperture effects as described in Section 2.2. Ages refer to mass-weighted stellar population ages in Myr, and A_V represents the total V -band attenuation in magnitudes. The parameters μ and δ_{ISM} describe, respectively, the fraction of total attenuation arising in the diffuse ISM and the slope of the ISM attenuation law.

redshift	N		$\langle \log M_* \rangle$ [M_\odot]	$\langle \log \text{SFR} \rangle$ [$M_\odot \text{ yr}^{-1}$]	$\langle \text{Age}_{\text{mass}} \rangle$ [Myr]	$\langle A_V \rangle$ [mag]	$\langle \mu \rangle$	$\langle \delta_{ISM} \rangle$
$3 \leq z < 4$	2327	Resolved	$8.96^{+0.77}_{-0.53}$	$0.7^{+0.7}_{-0.5}$	$268.2^{+46.5}_{-73.7}$	$0.92^{+0.11}_{-0.11}$	$0.44^{+0.01}_{-0.01}$	$-0.54^{+0.04}_{-0.04}$
		Integrated	$8.75^{+0.71}_{-0.57}$	$0.6^{+0.7}_{-0.5}$	$209.4^{+108.8}_{-141.9}$	$0.74^{+0.58}_{-0.58}$	$0.72^{+0.08}_{-0.06}$	$-0.61^{+0.14}_{-0.24}$
$4 \leq z < 5$	696	Resolved	$8.93^{+0.67}_{-0.45}$	$0.9^{+0.6}_{-0.4}$	$183.3^{+48.7}_{-78.9}$	$0.88^{+0.12}_{-0.12}$	$0.45^{+0.02}_{-0.01}$	$-0.50^{+0.04}_{-0.05}$
		Integrated	$8.72^{+0.63}_{-0.56}$	$0.8^{+0.6}_{-0.5}$	$130.5^{+103.9}_{-102.9}$	$0.64^{+0.55}_{-0.55}$	$0.74^{+0.10}_{-0.09}$	$-0.61^{+0.13}_{-0.21}$
$5 \leq z < 6$	272	Resolved	$8.98^{+0.66}_{-0.51}$	$1.0^{+0.6}_{-0.5}$	$159.5^{+23.1}_{-57.2}$	$0.91^{+0.12}_{-0.12}$	$0.45^{+0.01}_{-0.01}$	$-0.46^{+0.02}_{-0.05}$
		Integrated	$8.73^{+0.74}_{-0.60}$	$0.9^{+0.8}_{-0.6}$	$115.3^{+81.7}_{-91.0}$	$0.89^{+0.66}_{-0.66}$	$0.75^{+0.13}_{-0.08}$	$-0.55^{+0.16}_{-0.20}$
$6 \leq z < 7$	88	Resolved	$8.88^{+0.50}_{-0.37}$	$1.0^{+0.5}_{-0.3}$	$111.9^{+31.1}_{-37.4}$	$0.89^{+0.13}_{-0.13}$	$0.46^{+0.01}_{-0.01}$	$-0.46^{+0.04}_{-0.03}$
		Integrated	$8.60^{+0.61}_{-0.53}$	$1.0^{+0.5}_{-0.5}$	$55.6^{+91.2}_{-38.3}$	$0.80^{+0.65}_{-0.65}$	$0.81^{+0.09}_{-0.06}$	$-0.52^{+0.09}_{-0.15}$
$7 \leq z < 8$	15	Resolved	$9.37^{+0.25}_{-0.54}$	$1.5^{+0.2}_{-0.6}$	$110.7^{+3.9}_{-33.7}$	$1.21^{+0.15}_{-0.15}$	$0.46^{+0.01}_{-0.01}$	$-0.47^{+0.02}_{-0.03}$
		Integrated	$9.29^{+0.24}_{-0.72}$	$1.5^{+0.4}_{-0.8}$	$90.2^{+28.1}_{-69.1}$	$1.40^{+0.73}_{-0.73}$	$0.81^{+0.08}_{-0.13}$	$-0.40^{+0.07}_{-0.10}$
$8 \leq z < 9$	10	Resolved	$9.26^{+0.52}_{-0.26}$	$1.4^{+0.5}_{-0.3}$	$89.7^{+7.0}_{-7.7}$	$1.09^{+0.14}_{-0.14}$	$0.46^{+0.00}_{-0.01}$	$-0.46^{+0.04}_{-0.01}$
		Integrated	$9.10^{+0.49}_{-0.58}$	$1.3^{+0.7}_{-0.6}$	$70.4^{+26.1}_{-28.3}$	$1.18^{+0.73}_{-0.73}$	$0.82^{+0.06}_{-0.14}$	$-0.47^{+0.07}_{-0.19}$

tegrated fits. By performing SED fitting on spatially resolved scales, the analysis spatially disentangles heavily attenuated star-forming regions from older, less obscured stellar populations. This spatial separation breaks the age-dust degeneracy that affects integrated fits, where emission from young, bright stars in compact birth clouds can dominate the integrated light and mask the contribution from older stellar populations distributed more diffusely across galaxies.

The correlations between $\Delta \log M_\star \equiv \log\left(\frac{M_{\star, \text{resolved}}}{M_{\star, \text{integrated}}}\right)$ and the other parameters provide quantitative support for these trends (Figure 4). Across redshift bins, $\Delta \log M_\star$ shows the strongest linear correlation with the difference in mass-weighted stellar age (Pearson correlation coefficient $r = 0.78$, $p = 0.07$). A similarly strong correlation is found with the ISM attenuation slope difference ($r = 0.84$, $p = 0.04$), indicating that integrated fits assuming steeper attenuation laws reproduce the observed colors with insufficient A_V and overly young stellar ages, thereby yielding lower M/L ratios and underestimated stellar masses, whereas the resolved fits recover shallower slopes, higher attenuations, and correspondingly larger total stellar masses. Correlations with ΔA_V ($r = 0.68$, $p = 0.14$) and $\Delta\mu$ ($r = 0.36$, $p = 0.49$) suggest that variations in total attenuation and in the fraction of diffuse ISM attenuation contribute to the stellar mass offsets, though their influence appears less important than that of the slope and stellar ages. The weak dependence on $\Delta \log \text{SFR}$ ($r = 0.20$, $p = 0.70$) supports the interpretation that the discrepancies between resolved and integrated stellar masses are driven primarily by the combined effects of age-dependent

outshining and spatially inhomogeneous dust attenuation.

At higher redshifts ($z \gtrsim 5$), the age offset increases to 30%, though the absolute difference decreases to $\Delta \text{Age}_{\text{mass}} \approx 35$ Myr. This reflects both the younger overall stellar populations at these epochs (median ~ 110 Myr vs. ~ 265 Myr at $z < 4$) and the increasing photometric limitations as NIRCam filters no longer sample rest-frame NIR wavelengths. The mass offset remains significant at ~ 0.25 – 0.28 dex. These trends likely reflect the increasing limitations of the observed photometry (Whitler et al. 2023), as the rest-frame NIR is no longer sampled by NIRCam filters. The systematically younger stellar ages at $z > 5$ (median ~ 110 Myr vs. ~ 265 Myr at $z < 4$) reduce the contribution from older stellar populations, potentially mitigating outshining effects even as photometric constraints weaken. Without these longer-wavelength constraints, SED fits become dominated by rest-frame UV light from young stellar populations, enhancing outshining effects and reducing sensitivity to the older, more massive components. Consequently, both resolved and integrated fits converge toward younger ages and lower inferred A_V , with integrated fits remaining more affected by this bias.

Positive ΔA_V and $\Delta \text{Age}_{\text{mass}}$ values in Table 2, together with the resolved A_V – M_\star relation in Figure 3, indicate that attenuation and stellar age both increase toward regions of higher stellar mass, which mostly corresponds to the central parts of galaxies, supporting the presence of strong internal A_V and age gradients that are averaged out in integrated SED fits.

We find no significant dependence of the stellar mass offset on stellar metallicity, discussed in Section 3. The correla-

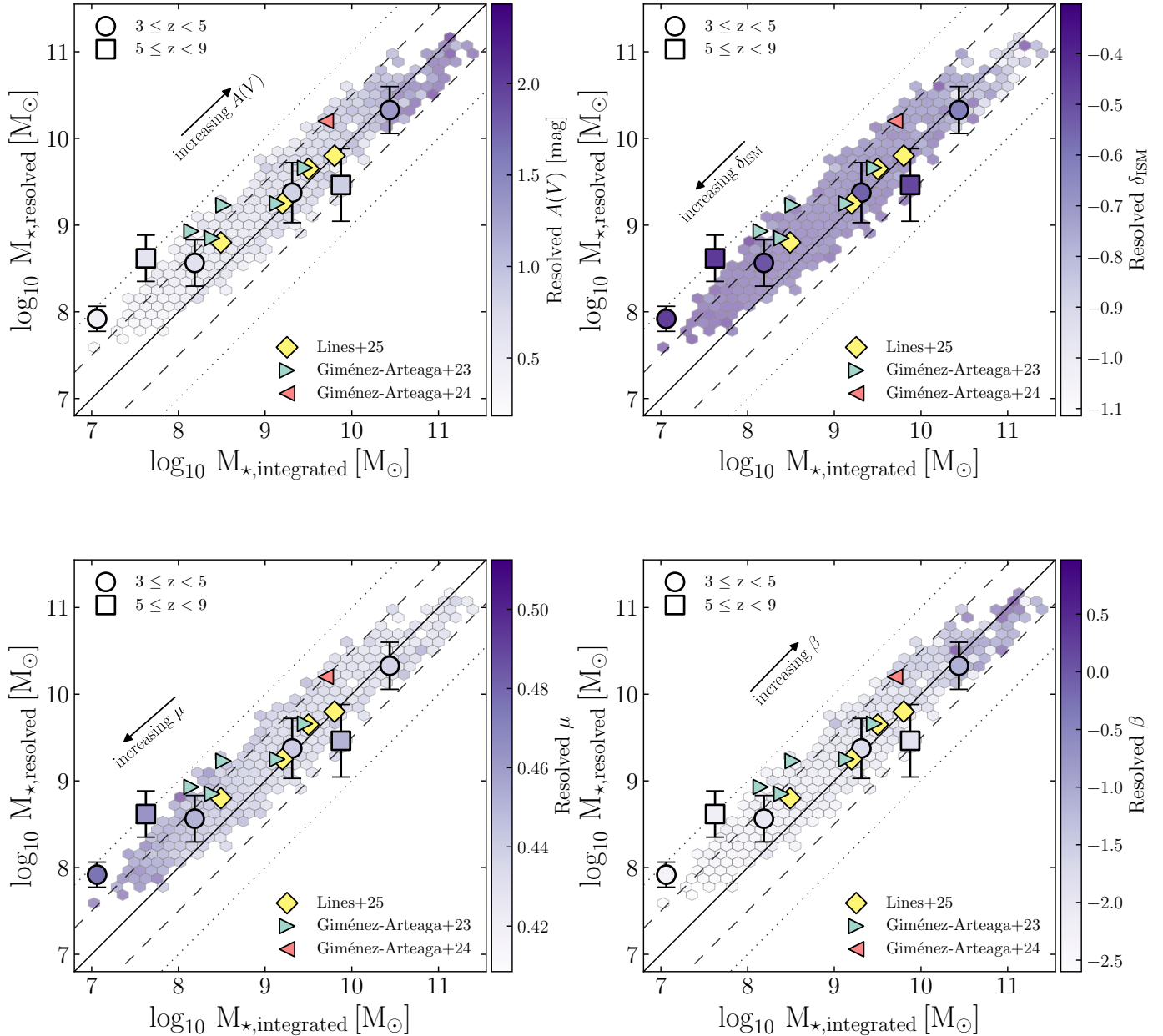


Fig. 4. Comparison between resolved and integrated stellar masses, corrected for aperture as described in Section 2.2, color-coded by the main attenuation parameters derived from the resolved SED fits: total A_V (top left), ISM attenuation slope δ_{ISM} (top right), μ (bottom left; the fraction of total attenuation arising in the diffuse ISM), and the UV continuum slope β (bottom right). Each panel shows the relation between $\log M_{*,resolved}$ and $\log M_{*,integrated}$ for galaxies at $3 \leq z < 5$ (circles) and $5 \leq z < 9$ (squares), with median binned values shown in color and error bars indicating the 1σ dispersion. Solid, dashed, and dotted lines mark the one-to-one relation and offsets of ± 0.5 and ± 1.0 dex, respectively. The arrow indicates the direction of increasing attenuation parameter. Yellow squares, turquoise triangles, and red triangles mark, respectively, the measurements from Lines et al. (2025), Giménez-Arteaga et al. (2023), and Giménez-Arteaga et al. (2024).

tion between $\Delta \log M_*$ and the stellar metallicity (Z_*) is weak ($r = 0.10$, $p < 10^{-3}$), indicating that variations in metallicity do not drive the differences between resolved and integrated stellar mass estimates. This is in line with works investigating stellar populations and SED (Shapley et al. 2001; Conroy 2013).

5. Summary & Conclusions

In this work, we conducted spatially resolved SED analysis of 3 408 mass-complete galaxies spanning $3 \leq z < 9$ in GOODS-South, utilizing deep JWST/NIRCam and HST/ACS observations. Our analysis quantifies systematic biases between

Table 3. Median differences in attenuation properties (resolved – integrated) in two resolved stellar mass bins.

Resolved $\log M_*$ [M $_{\odot}$]	N	ΔA_V [mag]	$\Delta \delta_{ISM}$	$\Delta \mu$
$7.5 \leq \log M_* < 9$	1846	+0.07	+0.10	-0.30
$9 \leq \log M_* < 11.5$	1562	+0.08	+0.08	-0.26

resolved and integrated stellar mass measurements and examines the role of dust geometry and stellar population properties in driving these discrepancies.

The resolved-to-integrated stellar mass comparison reveals a mass-dependent systematic offset. Low-mass systems ($\log M_\star/M_\odot < 8$) show the largest discrepancy at $\Delta \log M_\star = +0.34$ dex, which diminishes to $+0.22$ dex for $\log M_\star/M_\odot \sim 8.5$, then $+0.21$ dex at $\log M_\star/M_\odot \sim 9.5$, ultimately converging to near-unity ($+0.04$ dex) for the most massive galaxies ($\log M_\star/M_\odot \sim 10.5$). The sample-wide median offset of $\Delta \log M_\star = +0.24^{+0.16}_{-0.17}$ dex primarily reflects the intermediate-mass population ($\log M_\star \sim 8-10$) constituting 85% of our sample. This systematic trend confirms that low-mass galaxies suffer most severely from outshining-induced biases, with integrated methods underestimating true masses by factors of ~ 2 (0.3 dex). Conversely, massive systems ($\log M_\star > 10$) show excellent agreement between methods as older populations dominate their spectral signatures. These patterns arise from the interplay of outshining (Sorba & Sawicki 2018; Wuyts et al. 2013; Tacchella et al. 2022; Whitler et al. 2023) and heterogeneous dust distributions.

Systematic differences extend beyond mass to encompass dust and age parameters. Resolved measurements preferentially probe compact, dust-rich star-forming complexes (Chevance et al. 2020), yielding elevated attenuations (median $\Delta A_V \approx +0.08$ mag across mass bins) and reduced ISM dominance ($\Delta \mu$ from -0.30 to -0.26) relative to integrated estimates. The attenuation law slope exhibits graying ($\Delta \delta_{ISM} = +0.08$), reflecting clumpy birth cloud geometries, while integrated approaches smooth over these structures producing artificially steep slopes. Age determinations show parallel offsets: resolved mass-weighted ages systematically exceed integrated values (Wuyts et al. 2012), with integrated methods underestimating by 25% ($z < 5$) and 30% ($z \gtrsim 5$), corresponding to absolute differences of ≈ 56 Myr and ≈ 35 Myr respectively. This age bias reveals integrated fitting's systematic preference for young, luminous components.

Correlation analysis identifies primary drivers of mass discrepancies. The age offset shows the strongest correlation with $\Delta \log M_\star$ ($r = 0.78$, $p = 0.07$), confirming age-dependent outshining as a dominant mechanism. The ISM slope difference exhibits comparable correlation strength ($r = 0.84$, $p = 0.04$), demonstrating that integrated fitting's preference for steep attenuation curves leads to insufficient A_V , spuriously young ages, reduced mass-to-light ratios, and consequently underestimated masses. The ΔA_V correlation ($r = 0.68$, $p = 0.14$) further implicates dust geometry in shaping inferred parameters. Resolved fitting's ability to spatially separate heavily attenuated young populations in birth clouds from diffuse older populations breaks the age-dust degeneracy, enabling recovery of obscured stellar components contributing negligibly to integrated spectra.

At extreme redshifts ($z \gtrsim 5$), offsets diminish from $\sim 0.25-0.28$ dex ($z \lesssim 6$) to $\lesssim 0.1$ dex ($z > 7$), likely reflecting photometric limitations as NIRCam filters no longer sample rest-frame NIR wavelengths. Without long-wavelength constraints, fitting becomes UV-dominated, amplifying outshining while reducing sensitivity to massive, evolved populations. Both methods consequently converge toward younger ages and lower A_V , though integrated approaches remain more severely biased.

Key limitations include S/N-based pixel selection necessarily excluding low-signal regions, which preferentially samples luminous central zones potentially under-representing extended low-surface-brightness populations. Our aperture corrections assume similar mass-to-light ratios between detected and excluded regions; systematic age or dust differences could introduce uncertainties. JWST/NIRSpec spatially resolved spec-

troscopy would provide independent age and dust constraints, directly validating SED-derived parameters.

Practical recommendations for integrated SED fitting emerge from our analysis: expect mass-dependent systematic underestimation (~ 0.3 dex for $\log M_\star < 8$, ~ 0.2 dex at $\log M_\star \sim 8-10$, negligible beyond $\log M_\star > 10.5$). Integrated fitting preferentially adopts high μ values, over-emphasizing diffuse ISM attenuation. Lower μ priors (0.4–0.5) better capture birth cloud contributions, improving mass recovery. Flexible attenuation slopes enhance fitting quality, particularly for unresolved observations lacking direct dust geometry constraints.

Our findings demonstrate that systematic discrepancies between resolved and integrated stellar mass estimates fundamentally arise from the coupling of outshining with spatially varying dust attenuation geometry. Internal dust-light architecture must be considered when interpreting integrated SEDs, especially in low-mass, high-redshift regimes where biases are most pronounced. Resolved SED fitting, increasingly viable with JWST, offers a robust methodology for accurate mass determination while breaking age-dust degeneracies inherent to integrated approaches.

Acknowledgements. M.H. and P.G.P.-G. acknowledge support from grant PID2022-139567NB-I00 funded by Spanish Ministerio de Ciencia e Innovación MCIN/AEI/10.13039/501100011033, FEDER *Una manera de hacer Europa*. L.C. and S.A. acknowledge support from grant PID2021-127718NB-I00 funded by Spanish Ministerio de Ciencia e Innovación MCIN/AEI/10.13039/501100011033. A.J.B. and J.C. acknowledge funding from the “FirstGalaxies” Advanced Grant from the European Research Council (ERC) under the European Union’s Horizon 2020 research and innovation program (Grant agreement No. 789056). C.N.A.W. and Z.J. acknowledge support from JWST/NIRCam contract to the University of Arizona NAS5-02105. H.Ü. acknowledges funding by the European Union (ERC APEX, 101164796). Views and opinions expressed are however those of the authors only and do not necessarily reflect those of the European Union or the European Research Council Executive Agency. Neither the European Union nor the granting authority can be held responsible for them. E.C.-L. acknowledges support of an STFC Webb Fellowship (ST/W001438/1). C.W. acknowledges support from NOIRLab, which is managed by the Association of Universities for Research in Astronomy (AURA) under a cooperative agreement with the National Science Foundation. M.H. thanks Tiago Cortinhal for the discussions about computational optimization. This work is based on observations made with the NASA/ESA/CSA James Webb Space Telescope. The data were obtained from the Mikulski Archive for Space Telescopes at the Space Telescope Science Institute, which is operated by the Association of Universities for Research in Astronomy, Inc., under NASA contract NAS 5-03127 for JWST. The authors acknowledge the teams of programs 1895 and 1963 for developing their observing program with a zero-exclusive-access period. This work has made use of the Rainbow Cosmological Surveys Database, which is operated by the Centro de Astrobiología (CAB), CSIC-INTA.

References

- Abdullo'uf & Akiyama, M. 2018, MNRAS, 479, 5083
 Abraham, R. G., Ellis, R. S., Fabian, A. C., Tanvir, N. R., & Glazebrook, K. 1999, MNRAS, 303, 641
 Adams, N. J., Conselice, C. J., Ferreira, L., et al. 2023, MNRAS, 518, 4755
 Álvarez-Márquez, J., Crespo Gómez, A., Colina, L., et al. 2023, A&A, 671, A105
 Annunziatella, M., Pérez-González, P. G., Álvarez-Márquez, J., et al. 2025, A&A, 702, A224
 Battisti, A. J., Calzetti, D., & Chary, R. R. 2016, ApJ, 818, 13
 Beckwith, S. V. W., Stiavelli, M., Koekemoer, A. M., et al. 2006, AJ, 132, 1729
 Berkheimer, J. M., Carleton, T., Windhorst, R. A., et al. 2024, ApJ, 964, L29
 Bolzonella, M., Kovač, K., Pozzetti, L., et al. 2010, A&A, 524, A76
 Boquien, M., Burgarella, D., Roehlly, Y., et al. 2019, A&A, 622, A103
 Boquien, M., Duc, P. A., Galliano, F., et al. 2010, AJ, 140, 2124
 Bradley, L., Sipőcz, B., Robitaille, T., et al. 2024, astropy/phoutils: 2.0.2
 Brammer, G. B., van Dokkum, P. G., & Coppi, P. 2008, ApJ, 686, 1503
 Bruzual, G. & Charlot, S. 2003, MNRAS, 344, 1000
 Buat, V., Ciesla, L., Boquien, M., Małek, K., & Burgarella, D. 2019, A&A, 632, A79

- Buat, V., Noll, S., Burgarella, D., et al. 2012, *A&A*, 545, A141
- Bunker, A. J., Saxena, A., Cameron, A. J., et al. 2023, *A&A*, 677, A88
- Calzetti, D., Armus, L., Bohlin, R. C., et al. 2000, *ApJ*, 533, 682
- Calzetti, D., Kinney, A. L., & Storchi-Bergmann, T. 1994, *ApJ*, 429, 582
- Castellano, M., Fontana, A., Treu, T., et al. 2022, *ApJ*, 938, L15
- Chabrier, G. 2003, *PASP*, 115, 763
- Charlot, S. & Fall, S. M. 2000, *ApJ*, 539, 718
- Chevallard, J., Charlot, S., Wandelt, B., & Wild, V. 2013, *MNRAS*, 432, 2061
- Chevance, M., Kruijssen, J. M. D., Vazquez-Semadeni, E., et al. 2020, *Space Sci. Rev.*, 216, 50
- Cibinel, A., Le Floc'h, E., Perret, V., et al. 2015, *ApJ*, 805, 181
- Ciesla, L., Béthermin, M., Daddi, E., et al. 2020, *A&A*, 635, A27
- Ciesla, L., Boselli, A., Elbaz, D., et al. 2016, *A&A*, 585, A43
- Conroy, C. 2013, *ARA&A*, 51, 393
- da Cunha, E., Charlot, S., & Elbaz, D. 2008, *MNRAS*, 388, 1595
- de Barros, S., Schaerer, D., & Stark, D. P. 2014, *A&A*, 563, A81
- D'Eugenio, F., Pérez-González, P. G., Maiolino, R., et al. 2024, *Nature Astronomy*, 8, 1443
- Di Mascia, F., Gallerani, S., Ferrara, A., et al. 2021, *MNRAS*, 506, 3946
- Eisenstein, D. J., Johnson, B. D., Robertson, B., et al. 2025, *ApJS*, 281, 50
- Eisenstein, D. J., Willott, C., Alberts, S., et al. 2023, *arXiv e-prints*, arXiv:2306.02465
- Elbaz, D., Leiton, R., Nagar, N., et al. 2018, *A&A*, 616, A110
- Finkelstein, S. L., Bagley, M. B., Arrabal Haro, P., et al. 2022, *ApJ*, 940, L55
- Finkelstein, S. L., Bagley, M. B., Ferguson, H. C., et al. 2023, *ApJ*, 946, L13
- Finkelstein, S. L., Papovich, C., Salmon, B., et al. 2012, *ApJ*, 756, 164
- Fontana, A., D'Odorico, S., Poli, F., et al. 2000, *AJ*, 120, 2206
- Gallazzi, A. & Bell, E. F. 2009, *ApJS*, 185, 253
- García-Argumánez, Á., Pérez-González, P. G., Gil de Paz, A., et al. 2023, *ApJ*, 944, 3
- Giavalisco, M., Ferguson, H. C., Koekemoer, A. M., et al. 2004, *ApJ*, 600, L93
- Giménez-Arteaga, C., Fujimoto, S., Valentino, F., et al. 2024, *A&A*, 686, A63
- Giménez-Arteaga, C., Oesch, P. A., Brammer, G. B., et al. 2023, *ApJ*, 948, 126
- Gómez-Guijarro, C., Magnelli, B., Elbaz, D., et al. 2023, *A&A*, 677, A34
- Hamed, M., Ciesla, L., Béthermin, M., et al. 2021, *A&A*, 646, A127
- Hamed, M., Małek, K., Buat, V., et al. 2023a, *A&A*, 674, A99
- Hamed, M., Pisticci, F., Figueira, M., et al. 2023b, *A&A*, 679, A26
- Harvey, T., Conselice, C. J., Adams, N. J., et al. 2025, *MNRAS*, 542, 2998
- Hemmati, S., Miller, S. H., Mobasher, B., et al. 2014, *ApJ*, 797, 108
- Iani, E., Caputi, K. I., Rinaldi, P., et al. 2024, *ApJ*, 963, 97
- Illingworth, G., Magee, D., Bouwens, R., et al. 2016, *arXiv e-prints*, arXiv:1606.00841
- Inoue, A. K. 2011, *MNRAS*, 415, 2920
- Jafarizayani, M., Mobasher, B., Hemmati, S., et al. 2019, *ApJ*, 887, 204
- Jain, S., Tacchella, S., & Mosleh, M. 2024, *MNRAS*, 527, 3291
- Kriek, M. & Conroy, C. 2013, *ApJ*, 775, L16
- Lanyon-Foster, M. M., Conselice, C. J., & Merrifield, M. R. 2012, *MNRAS*, 424, 1852
- Lee, J. C., Whitmore, B. C., Thilker, D. A., et al. 2022, *ApJS*, 258, 10
- Li, J., Da Cunha, E., González-López, J., et al. 2024, *ApJ*, 976, 70
- Lines, N. E. P., Bowler, R. A. A., Adams, N. J., et al. 2025, *MNRAS*, 539, 2685
- Lisiecki, K., Donevski, D., Man, A. W. S., et al. 2025, *arXiv e-prints*, arXiv:2509.10117
- Lo Faro, B., Buat, V., Roehlly, Y., et al. 2017, *MNRAS*, 472, 1372
- Looser, T. J., D'Eugenio, F., Maiolino, R., et al. 2025, *A&A*, 697, A88
- Luo, B., Brandt, W. N., Xue, Y. Q., et al. 2017, *ApJS*, 228, 2
- Maiolino, R., Risaliti, G., Signorini, M., et al. 2025, *MNRAS*, 538, 1921
- Małek, K., Bankowicz, M., Pollo, A., et al. 2017, *A&A*, 598, A1
- Małek, K., Buat, V., Roehlly, Y., et al. 2018, *A&A*, 620, A50
- Maraston, C., Pforr, J., Renzini, A., et al. 2010, *MNRAS*, 407, 830
- Markov, V., Gallerani, S., Ferrara, A., et al. 2025, *Nature Astronomy*, 9, 458
- Martinache, F., Ceau, A., Laugier, R., et al. 2020, *A&A*, 636, A72
- Martorano, M., van der Wel, A., Baes, M., et al. 2025, *A&A*, 694, A76
- Matharu, J., Nelson, E. J., Brammer, G., et al. 2024, *A&A*, 690, A64
- Matsuura, M., Boyer, M., Arendt, R. G., et al. 2024, *MNRAS*, 532, 3625
- McLure, R. J., Dunlop, J. S., Cullen, F., et al. 2018, *MNRAS*, 476, 3991
- Merlin, E., Santini, P., Paris, D., et al. 2024, *A&A*, 691, A240
- Mitchell, P. D., Lacey, C. G., Baugh, C. M., & Cole, S. 2013, *MNRAS*, 435, 87
- Morishita, T., Ichikawa, T., Noguchi, M., et al. 2015, *ApJ*, 805, 34
- Naidu, R. P., Oesch, P. A., van Dokkum, P., et al. 2022, *ApJ*, 940, L14
- Narayanan, D., Conroy, C., Davé, R., Johnson, B. D., & Popping, G. 2018, *ApJ*, 869, 70
- Narayanan, D., Lower, S., Torrey, P., et al. 2024, *ApJ*, 961, 73
- Navarro-Carrera, R., Rinaldi, P., Caputi, K. I., et al. 2024, *ApJ*, 961, 207
- Noll, S., Burgarella, D., Giovannoli, E., et al. 2009, *A&A*, 507, 1793
- Oesch, P. A., Brammer, G., Naidu, R. P., et al. 2023, *MNRAS*, 525, 2864
- Osborne, C. & Salim, S. 2024, *ApJ*, 962, 59
- Pacucci, F., Nguyen, B., Carniani, S., Maiolino, R., & Fan, X. 2023, *ApJ*, 957, L3
- Papovich, C., Dickinson, M., & Ferguson, H. C. 2001, *ApJ*, 559, 620
- Pérez-González, P. G., Barro, G., Annunziatella, M., et al. 2023, *ApJ*, 946, L16
- Pérez-González, P. G., Östlin, G., Costantin, L., et al. 2025, *ApJ*, 991, 179
- Pforr, J., Maraston, C., & Tonini, C. 2012, *MNRAS*, 422, 3285
- Pierini, D., Gordon, K. D., Witt, A. N., & Madsen, G. J. 2004, *ApJ*, 617, 1022
- Polletta, M., Frye, B. L., Garuda, N., et al. 2024, *A&A*, 690, A285
- Pozzetti, L., Bolzonella, M., Zucca, E., et al. 2010, *A&A*, 523, A13
- Qin, J., Zheng, X. Z., Wuyts, S., et al. 2024, *MNRAS*, 528, 658
- Rieke, M. J., Robertson, B., Tacchella, S., et al. 2023, *ApJS*, 269, 16
- Rogers, A. B., McLure, R. J., & Dunlop, J. S. 2013, *MNRAS*, 429, 2456
- Sabti, N., Muñoz, J. B., & Kamionkowski, M. 2024, *Phys. Rev. Lett.*, 132, 061002
- Salim, S., Boquien, M., & Lee, J. C. 2018, *ApJ*, 859, 11
- Salim, S. & Narayanan, D. 2020, *ARA&A*, 58, 529
- Shapley, A. E., Steidel, C. C., Adelberger, K. L., et al. 2001, *ApJ*, 562, 95
- Shen, L., Papovich, C., Matharu, J., et al. 2024, *ApJ*, 963, L49
- Shivaei, I., Darvish, B., Sattari, Z., et al. 2020a, *ApJ*, 903, L28
- Shivaei, I., Naidu, R. P., Rodríguez Montero, F., et al. 2025, *arXiv e-prints*, arXiv:2509.01795
- Shivaei, I., Reddy, N., Rieke, G., et al. 2020b, *ApJ*, 899, 117
- Song, J., Fang, G., Lin, Z., Gu, Y., & Kong, X. 2023, *ApJ*, 958, 82
- Sorba, R. & Sawicki, M. 2015, *MNRAS*, 452, 235
- Sorba, R. & Sawicki, M. 2018, *MNRAS*, 476, 1532
- Speagle, J. S., Steinhardt, C. L., Capak, P. L., & Silverman, J. D. 2014, *ApJS*, 214, 15
- Suess, K. A., Leja, J., Johnson, B. D., et al. 2022, *ApJ*, 935, 146
- Tacchella, S., Carollo, C. M., Renzini, A., et al. 2015, *Science*, 348, 314
- Tacchella, S., Finkelstein, S. L., Bagley, M., et al. 2022, *ApJ*, 927, 170
- Topping, M. W., Stark, D. P., Endsley, R., et al. 2022, *MNRAS*, 516, 975
- Trayford, J. W., Lagos, C. d. P., Robotham, A. S. G., & Obreschkow, D. 2020, *MNRAS*, 491, 3937
- Walcher, J., Groves, B., Budavári, T., & Dale, D. 2011, *Ap&SS*, 331, 1
- Wang, B., Leja, J., Labbé, I., et al. 2024, *ApJS*, 270, 12
- Wang, X., Jones, T., Vulcani, B., et al. 2022, *ApJ*, 938, L16
- Weibel, A., Oesch, P. A., Barrufet, L., et al. 2024, *MNRAS*, 533, 1808
- Whitler, L., Stark, D. P., Endsley, R., et al. 2023, *MNRAS*, 519, 5859
- Wild, V., Kauffmann, G., Heckman, T., et al. 2007, *MNRAS*, 381, 543
- Williams, C. C., Tacchella, S., Maseda, M. V., et al. 2023, *ApJS*, 268, 64
- Witten, C., McClymont, W., Laporte, N., et al. 2025, *MNRAS*, 537, 112
- Wuyts, S., Förster Schreiber, N. M., Genzel, R., et al. 2012, *ApJ*, 753, 114
- Yan, H., Ma, Z., Ling, C., Cheng, C., & Huang, J.-S. 2023, *ApJ*, 942, L9
- Zibetti, S., Charlot, S., & Rix, H.-W. 2009, *MNRAS*, 400, 1181

Appendix A: SFH parametrization

To explore the impact of SFH assumptions on our results, we tested several commonly used parametric SFH models, including constant, delayed, and delayed with an optional recent burst in the last 100 Myr. Our goal was to assess whether the choice of SFH significantly affects the stellar mass differences between resolved and integrated SED fits. For each SFH scenario (with parameters outlined in Table A.1), we performed SED fitting using the same dataset and configuration, and compared the resulting $\Delta \log M_\star$ values. We also tested variations in the minimum stellar population age allowed for the stellar population, including cutoffs at 10, 25, 50, and 100 Myr, in order to test its consequence on amplifying the outshining bias.

We found that the overall trends and mass discrepancies between resolved and integrated fits were broadly consistent across these choices. The median values of $\Delta \log M_\star$ for the constant SFH using cutoffs of 10 and 25 Myr were among the highest, at 0.29 and 0.30 dex respectively, while the delayed SFH also yielded a similarly high offset of 0.30 dex. The lowest offset was obtained with the delayed + burst model (0.16 dex). The difference between the highest and lowest median $\Delta \log M_\star$ across all configurations is 0.14 dex. We adopted a constant SFH with a minimum age of 50 Myr for our final modeling, as it yielded an intermediate offset (0.24 dex) and the lowest scatter among all tested configurations ($\sigma = 0.18$ dex, compared to $\sigma = 0.21$ dex for constant with 10 Myr cutoff and $\sigma = 0.23$ dex for delayed + burst). Additionally, the constant SFH has fewer free parameters than delayed or burst models, making it computationally efficient, which was a practical consideration given the large number of pixels fitted in our resolved analysis. This choice also helped mitigate possible outshining biases by avoiding the need to populate galaxies with very young stellar ages, which can dominate the light. These results are illustrated in Figure A.1. This finding is supported by spectro-photometric studies which demonstrate that stellar mass estimates are robust to variations in SFH assumptions (Annunziatella et al. 2025).

Appendix B: Comparisons between SED fitting approaches

To assess how different measurement approaches influence the derived stellar properties, we applied both resolved and integrated SED analyses to each galaxy in our sample. In the integrated approach, total fluxes were obtained by summing the pixels that satisfy our predefined S/N and band coverage thresholds (Section 2), ensuring consistency with the resolved analysis. The resolved approach was constructed by summing the best-fit pixel-by-pixel SEDs, which were then compared directly to the integrated SEDs for each galaxy.

For reference, we also considered aperture photometry from Merlin et al. (2024), corresponding to standard one-dimensional fitting applied to the total flux measured within a large aperture encompassing the full galaxy. The stellar masses derived from both the resolved and integrated analyses were scaled using aperture-based corrections to ensure that all measurements refer to the same total enclosed flux.

Figure B.1 illustrates the comparison between these two approaches for a representative galaxy. The spatially resolved property maps (left panels) reveal strong internal gradients: stellar mass and dust attenuation (A_V) are centrally concentrated, mass-weighted ages increase toward the galaxy center, and the ISM attenuation slope (δ_{ISM}) varies spatially across the galaxy. These gradients demonstrate the internal heterogeneity that is averaged

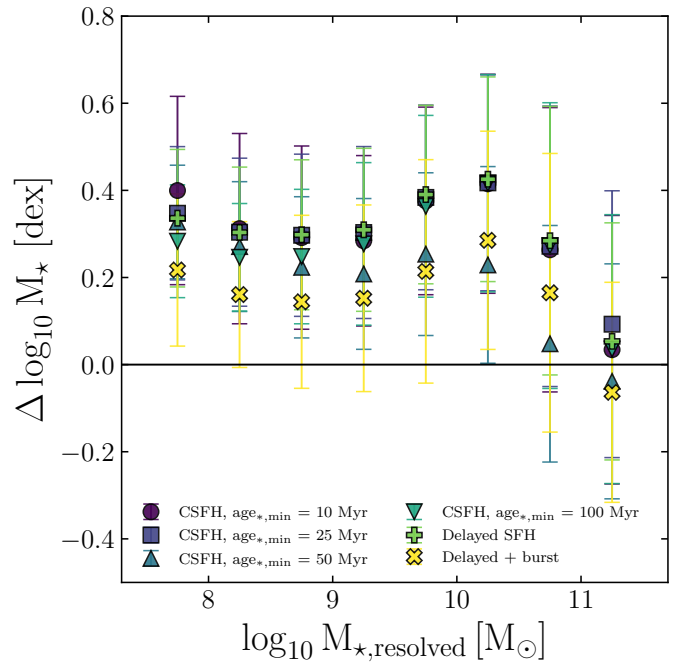


Fig. A.1. Difference between resolved and integrated stellar masses as a function of resolved stellar mass, for different SFH assumptions. Error bars indicate the 16th-84th percentile range in each bin. Results are shown for constant SFHs (CSFH) with minimum stellar ages of 10, 25, 50, and 100 Myr, delayed SFH, and delayed + burst SFH.

over in integrated fitting. Both the resolved and integrated approaches (right panels) provide good fits to the observed photometry, but yield systematically different physical parameters.

Table A.1. Summary of input parameters for the various SFH scenarios tested in the SED fitting using CIGALE. Each SFH model was applied independently to assess the robustness of our results. All other components of the SED modeling, such as dust attenuation, nebular emission, and stellar population synthesis, were held fixed and consistent with the configuration listed in Table 1. The values were linearly spaced.

Parameter	Priors
	Constant SFH
age _* [Myr]	100 values in [10-2000] 100 values in [25-2000] 100 values in [50-2000] 100 values in [100-2000]
	Delayed SFH
τ^i [Myr]	20 values in [100-6000]
age _* [Myr]	100 values in [50-2000]
	Delayed SFH + recent burst
τ_{main} [Myr]	20 values in [100-6000]
τ_{burst}^{ii} [Myr]	5 values in [50-500]
f_{burst}^{iii}	0%, 1%, 5%, 10%
age _* [Myr]	100 values in [50-2000]
age _{burst} [Myr]	10, 25, 50

ⁱ e-folding time of the main stellar population.

ⁱⁱ e-folding time of the late stellar population.

ⁱⁱⁱ Mass fraction of the late burst population.

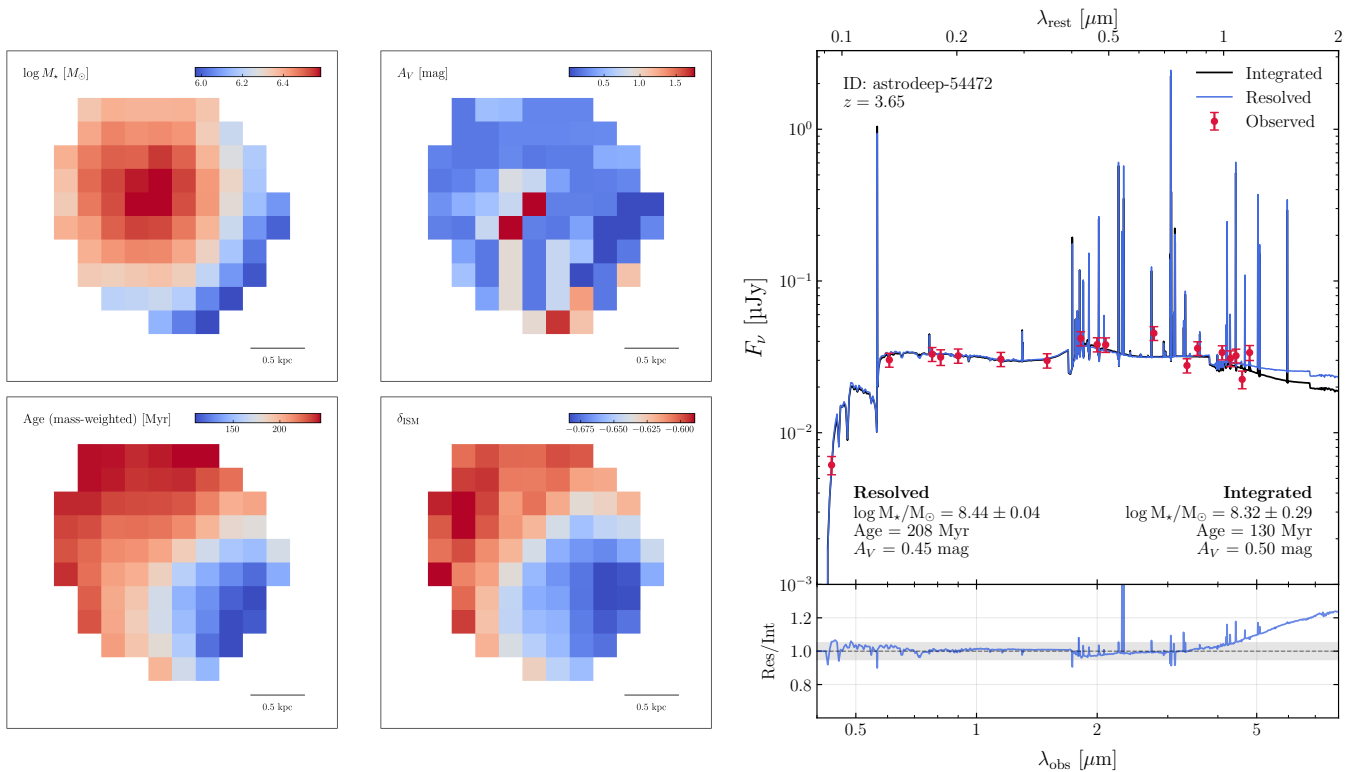


Fig. B.1. Resolved properties and SED comparison for galaxy astrodeep-54472 at $z = 3.65$. **Left:** Spatially resolved maps of stellar mass, A_V , mass-weighted age, and δ_{ISM} from pixel-by-pixel SED fitting, revealing strong central concentrations of mass and attenuation, age gradients, and spatial variations in attenuation slope. **Right (top):** Observed photometry (red points) compared to integrated (black) and summed resolved (blue) SED models. The gold shaded region shows flux differences between methods. Resolved fitting recovers higher stellar mass (8.44 vs 8.32 dex) and older age (208 vs 130 Myr). **Right (bottom):** Ratio of resolved to integrated SEDs (Res/Int); dashed line marks unity, gray band shows $\pm 5\%$. This example illustrates how spatial gradients in dust and stellar populations, visible in resolved analysis, are averaged out in integrated fits, leading to systematically lower mass and age estimates.

The resolved approach, which utilizes spatial information at the pixel level, recovers a higher stellar mass (0.12 dex) and older mass-weighted age ($\sim 60\%$ older) compared to the integrated approach that treats the galaxy as a single unresolved source. This example demonstrates the key systematic differences that persist across our full sample, which are quantified statistically in Section 4.

Appendix C: Mock analysis

To evaluate the reliability of the derived physical parameters, we performed a mock analysis using the best-fit SEDs from our main fitting run. Specifically, for each galaxy, synthetic photometric fluxes were generated based on the best-fit model in the observed bands and then perturbed with random Gaussian noise consistent with the measurement uncertainties in the original catalog. This mock photometry was subsequently refitted using the same configuration as the original analysis. By comparing the input (exact) and recovered (estimated) physical parameters, such as stellar mass, SFR, and attenuation, we obtain an empirical estimate of the typical uncertainties and potential biases associated with the adopted SED modeling setup. This provides a crucial test of the internal consistency and robustness of our fitting approach (Boquien et al. 2019; Osborne & Salim 2024).

The results of the mock analysis are illustrated in Figure C.1. Each panel compares a key physical parameter (e.g., stellar

mass, SFR, age, dust attenuation properties, and the attenuation slope) estimated using both integrated and spatially resolved SED fitting. Overall, most parameters show strong correlations with their exact input values, particularly stellar mass and SFR, which are recovered with high fidelity ($\rho \approx 0.99$ for integrated and $\rho \approx 0.93$ for resolved fits). Some parameters, such as the attenuation slope and ISM attenuation exhibit larger scatter, especially in the resolved case. This is expected, as these prior parameters are more sensitive to local variations in S/N and spectral coverage, and may suffer from degeneracies with age and SFH shape. Nonetheless, the recovered values of the stellar mass and SFR follow the one-to-one relation, indicating that our SED fitting setup is capable of reproducing the input parameters across a wide range of physical conditions. This validates the robustness of our modeling framework for both integrated and resolved analyses, while also rendering the computations less expensive.

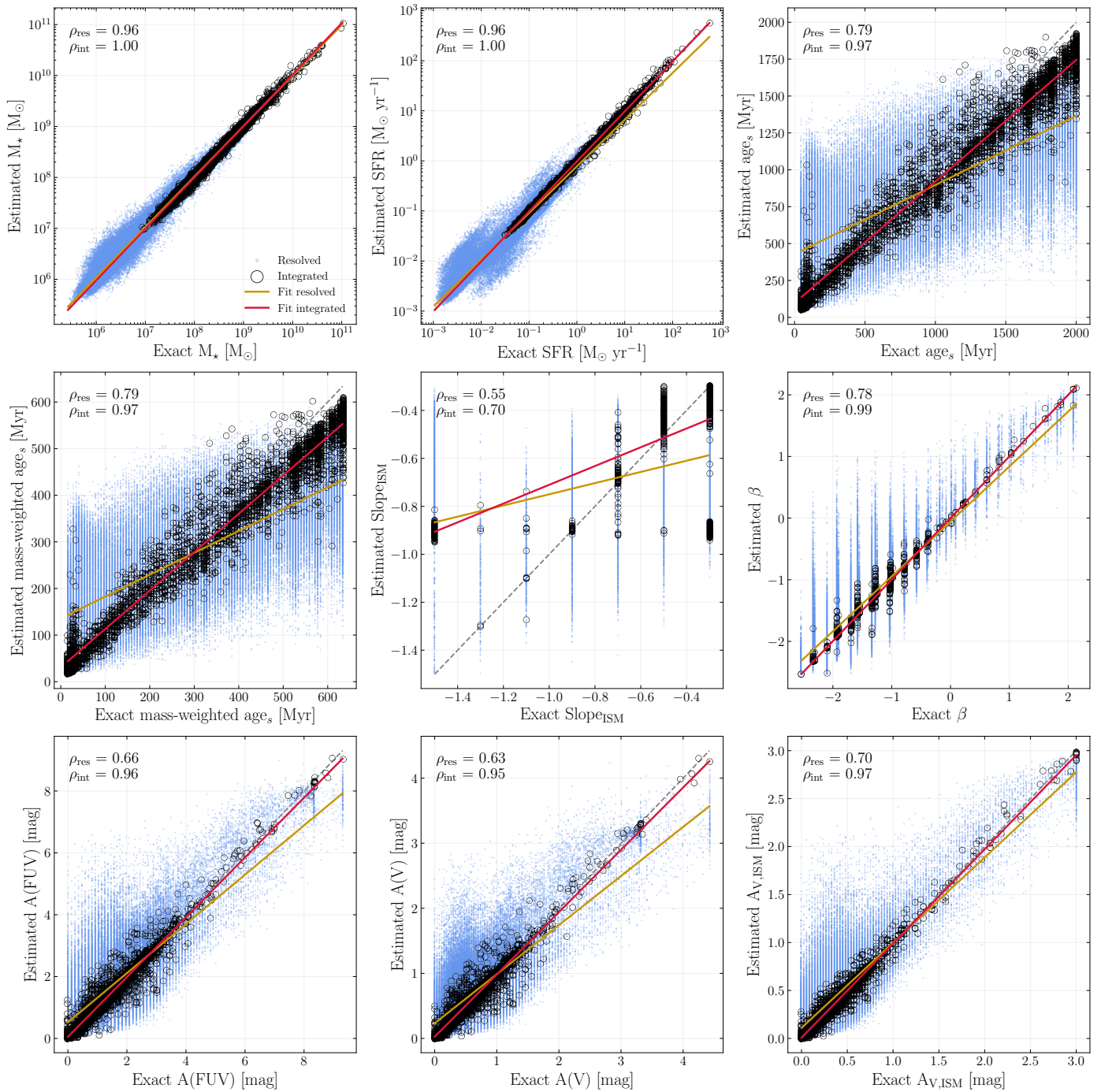


Fig. C.1. Comparison between the exact input values (x-axis) and the recovered mock values (y-axis) derived from the mock analysis of the resolved (blue crosses) and integrated (yellow dots). Each point represents the probability weighted mean of the posterior distribution for a given parameter. The stellar mass, SFR, and the β UV slope are all a result of SED fitting. The other parameters, namely the ages, the attenuation slopes and the attenuation values in the ISM are all priors for the SED fitting process. The black dashed line indicates the one-to-one relation. The red and blue solid lines represent linear fits to the integrated and resolved results, respectively. Spearman's rank correlation coefficients (ρ) for each fit are indicated in the legend of each panel.